Fast Flux Maps Computation of Synchronous Reluctance Machines With and Without Permanent Magnets Assistance

Gianvito Gallicchio, *Member, IEEE*, Mauro Di Nardo, *Member, IEEE*, Francesco Cupertino, *Senior Member, IEEE*
Vasyl Varvolik, *Graduate Student Member, IEEE*, Giampaolo Buticchi, *Senior Member, IEEE*
Michele Degano, *Senior Member, IEEE* and Chris Gerada, *Senior Member, IEEE*

***Abstract*—This paper proposes a computational efficient and accurate hybrid analytical-finite element (FE) performance prediction methodology for synchronous reluctance (SyR) machines. The hybrid procedure consists in solving the d- and q-axis magnetic equivalent circuits in a non-linear fashion so to consider the saturation effects of both stator and rotor iron parts. The cross-coupling effects are taken into account by adjusting the analytical flux maps with the results obtained FE-simulating few operating points in the d-q current plane. The proposed approach allows to obtain an excellent estimation of the direct and quadrature axis fluxes for a wide range of operating conditions including the overload ones with a negligible computational effort when compared to a full FE analysis. The estimation accuracy has been assessed analysing a wide spectrum of SyR machine geometries featuring different stator slots and flux barriers combinations including a PM-assisted variant. A sensitivity analysis shows the trade-off between estimation accuracy and computational time while leveraging on the discretization of the airgap equivalent magnetic circuit. The proposed fast performance estimation method is finally validated against the experimental measurements carried out on a SyR machine prototype.**

***Index Terms*—Cross coupling, finite element analysis, flux map, interior permanent magnet, magnetic equivalent circuit, magnetic model, permanent magnet assisted, saturation, synchronous reluctance machine.**

I. Introduction

THE design of an electrical machine is a challenging engineering task because several indexes have to be simultaneously considered to assess all the performance trade-offs while identifying the geometry and selecting the constituent materials [1]. This task becomes even more challenging when the considered application continuously works in different operating conditions - as in traction applications - thus requiring the evaluation of the same performance index in several operating points [2], [3]. The design is further complicated when dealing with machine topology with a high non-linear behaviour and a complex geometry [4]. The practical consequence of having a wide set of requirements and objectives when designing electrical machines with a high non-linear behaviour and a complex geometry is the impressively high computational burden [5]. Indeed, the non-linear behaviour implies the need of adopting an accurate performance estimation methodology which is usually computational expensive. The high number of parameters required to describe a complex structure makes the design process longer whatever approach is adopted for the optimization or the sensitivity analysis [6].

One of the most commonly adopted solution in many applications, including traction, is the permanent magnet assisted synchronous reluctance (PMaSyR) machine [7] which has both non-linear magnetic behaviour and a complex rotor geometry [8] as shown in Fig. 1. The evaluation of the machine performance over a complex driving cycle requires the knowledge of the machine behaviour - flux-current relation and electromagnetic losses - under a wide range of current supplies, i.e. d-q current combinations [9]. The finite element method is surely able of considering all the non-linearity along with the effects of the small geometrical features (e.g. slot opening, tooth shoe etc.), but it makes the complete computation of the flux-current map computationally too expensive especially when this evaluation has to be performed for many geometries. Analytical approaches [10]–[12] based on linear magnetic equivalent circuits (MECs) have the clear advantage

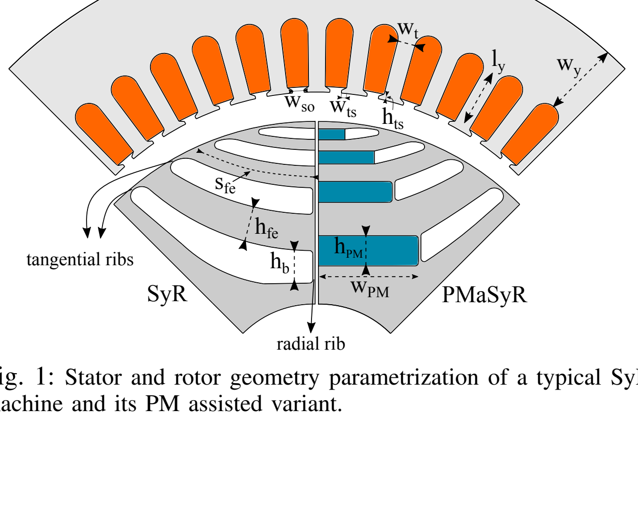

Fig. 1: Stator and rotor geometry parametrization of a typical SyR machine and its PM assisted variant.

G. Gallicchio, M. Di Nardo and F. Cupertino are with the Department of Electrical Engineering and Information Technology, Politecnico di Bari, Bari, 70126 Italy (e-mail: gianvito.gallicchio@poliba.it, mauro.dinardo@poliba.it, francesco.cupertino@poliba.it)

V. Varvolik and G. Buticchi are with the Zhejiang Key Laboratory for More Electric Aircraft Technologies, University of Nottingham Ningbo China. Ningbo, 315100 China. (e-mail: vasyl.varvolik@nottingham.edu.cn, buticchi@ieee.org

M. Degano and C. Gerada are with the Power Electronics, Machines and Control Group, University of Nottingham, Nottingham, NG7 2RD, UK. (e-mail: michele.degano@nottingham.ac.uk, chris.gerada@nottingham.ac.uk)

of the fast resolution but comes at the cost of low accuracy given their inability to account for the saturation and cross-saturation. As a result, these approaches are not able to estimate the machine flux maps; instead, they are often employed to estimate performance at a single, non-saturated operating point and to determine design parameters for machines that mostly operate in that single operating condition. A non-linear analytical model has been proposed in [13] based on the use of a unique parametric magnetic equivalent circuit for both d-axis and q-axis flux paths. The initial linear solution in terms of airgap flux density is corrected to account the saturation effect by calculating an equivalent airgap length function of the angular coordinate; this allows achieving an overall good performance estimation. However, the accurate modeling of the cross-saturation heavily depends on the way the rotor equivalent circuit is built and in particular on the level of discretization of the flux paths. It can be roughly stated that the higher the number of nodes of the rotor equivalent circuit, the higher the model accuracy. When the discretization level becomes independent from the underlying geometry, the modelling becomes non-parametric [14]. The latter approach, i.e. non-parametric MEC, allows obtaining an overall excellent estimation of the magnetic fields within the machine with a reduced, but still moderate, computational burden if compared with the FE approach [15]. Such method has been adopted for the analysis of a single machine design, and not within a systematic design procedure given its computational cost [16]. Another performance estimation methodology consists of adopting two different parametric circuits, one for the d-axis flux path and other for the q-axis one [17]. This approach allows to drastically reduce the problem complexity in terms of number of MEC nodes and so the computational time without neglecting the saturation when implemented in a non-linear fashion. Obviously this approach does not allow to account for the cross-coupling effect as the equivalent circuits model only the d- and the q-axis flux paths [18]. The idea of separating the two magnetic circuits is effective since the complexity of the geometry (i.e. placement of structural iron ribs, PMs, flux barrier shape, etc.) does not affect the complexity of the magnetic circuits, which can be therefore generalized regardless the stator and rotor geometries. In fact, the PM and iron ribs can be neglected in the d-axis circuit, whereas they can be considered always in parallel to each other in the q-axis one whenever they are more than one per barrier (i.e. the number of nodes does not increase with the rotor ribs or PM pieces per barrier). On the contrary, when adopting a unique magnetic circuit for every supply condition, the rotor circuit part heavily depends on the considered geometry since it has to be able to model all flux paths and related cross-saturation [19].

With the aim of joining the advantage of the light computational cost of two separate parametric MECs and the accuracy of the FE analysis in accounting also the cross-saturation, this work proposes a hybrid analytical-FE modeling approach of a generic PMaSyR machine extending the work [20]. In particular, the d- and q-axis flux paths are modeled by two non-linear equivalent magnetic circuits to correctly and directly evaluate the saturation effects. Then, few static FEAs are carried out to adjust the estimations of the flux map in the d-q current plane so take into account the cross-coupling effects. Particular emphasis is placed on the description of the two general MECs able to model any number of slots, poles and rotor flux barriers with the aid of an enhanced airgap model along with the details of FE-adjustment procedure.

The paper is organised as follows. Section II reports a detailed description of the analytical procedure, whereas the results of its applications and its limits are shown in section III. A sensitivity analysis is reported assessing the trade-off between estimation accuracy and computational time while leveraging on the discretization of the airgap equivalent magnetic circuit. Section IV describes the FE-correction procedure for both SyR machine and PM-assisted variant, whereas the test bench setup as well as the identification results are reported in Section V.

II. Non-linear magnetic equivalent circuits

The torque produced by a PMaSyRMs can be expressed in terms of currents and flux linkages according to the well-known equation (1):

$$T = \frac{3}{2}p[\lambda_d(i_d, i_q)i_q - \lambda_q(i_d, i_q)i_d] \tag{1}$$

where p is the number of pole pairs, i_d and i_q are the d- and q-axis currents, λ_d and λ_q are the d- and q-axis flux linkages which are both non-linear function of both i_d and i_q. The internal power factor, defined by the sine of the angular displacement between the current and flux linkage vectors, can be written as:

$$ipf = \sin\left[\arctan\left(\frac{i_q}{i_d}\right) - \arctan\left[\frac{\lambda_q(i_d, i_q)}{\lambda_d(i_d, i_q)}\right]\right] \tag{2}$$

It follows that the correct estimation of these two performance indexes depends on the accuracy of the flux linkages calculation in any operating conditions. The correct definition of the d- and q-axis magnetic circuits heavily depends on stator and rotor layouts, which include the number of flux barriers, their size and position and the number of stator slots per pole per phase. An example of the flux paths obtained when d-axis (a) or q-axis (b) current is applied is reported in Fig. 2. As well known, in the first case, the flux tubes follow the rotor flux guides, cross the airgap and the stator teeth and yokes; differently, the q-axis flux path crosses the flux barriers leading to different magnetic potentials of the rotor islands.

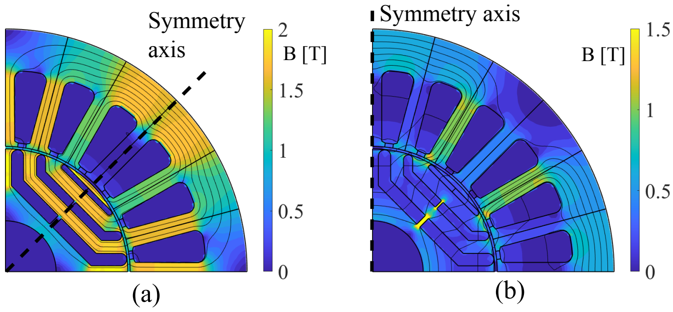

Fig. 2: d-axis (a) and q-axis (b) flux paths.

In the following subsections, first the MECs are described when supplying only with d- or q-axis current. Then, a general circuital model of the interface between the stator and the rotor is presented before detailing the overall non-linear MEC resolution.

A. d-axis MEC

The magnetic equivalent circuits shown in Fig. 3 provides an accurate lumped-parameters description of the main flux paths circulating in the machine when supplied with only d-axis current. Only half-pole is considered thanks to the rotor symmetry.

The MEC is divided into three parts, namely the stator, the rotor and the airgap.

The stator is modeled by a permeance $\mathscr{P}^i_{sy}$ in parallel to a flux generator φ^i for each yoke piece, a permeance for each tooth $\mathscr{P}^i_{st}$ and two permeance modeling the tooth shoe $\mathscr{P}^i_{ts}$ and slot opening parts $\mathscr{P}^i_{so}$. The flux generators φ^i can be obtained as in (3):

$$\varphi^i = F^i \cdot \mathscr{P}^i_{sy} \tag{3}$$

where F_i is the magnetomotive force of each yoke which is a function of the phase currents and can be calculated as in (4):

$$\mathbf{F} = z_Q \mathbf{MI} \tag{4}$$

where $\mathbf{F} = [F^1 \quad F^2 \quad ... \quad F^{n_s}]'$, $I = [i_a \quad i_b \quad i_c]'$ when considering a three-phase machine and $\mathbf{M}$ is a $[n_s$ x 3$]$ matrix representing the position of the phase coils, n_s is half of the number of slots per pole and z_Q is the slot conductors number. The currents vector I can be obtained considering the d-axis supply (i.e $\mathbf{i}_{dq} = i_d$) and applying the well-known Park transformation. The following expressions can be used for the calculation of the several stator related permeance:

$$\mathscr{P}^i_{sy} = \frac{\mu_0 \cdot \mu^i_{fe-sy} \cdot w_y}{l_y} l_{fe} \quad \text{for} \quad \text{i} = 1, 2, ..., n_s \tag{5}$$

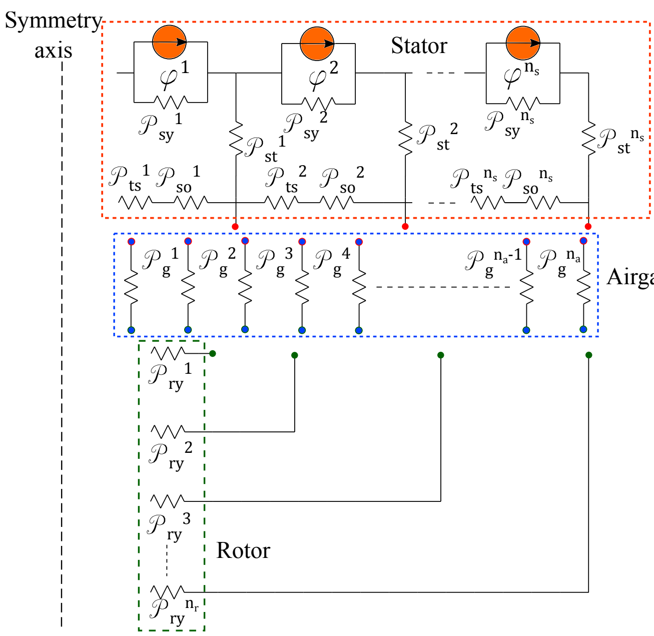

Fig. 3: Magnetic equivalent circuit for the d-axis flux path.

$$\mathscr{P}^i_{st} = \frac{\mu_0 \cdot \mu^i_{fe-st} \cdot w_t}{l_t} l_{fe} \quad \text{for} \quad \text{i} = 1, 2, ..., n_s \tag{6}$$

$$\mathscr{P}^i_{ts} = \frac{\mu_0 \cdot \mu^i_{fe-ts} \cdot h_{ts}}{w_{ts}} l_{fe} \quad \text{for} \quad \text{i} = 1, 2, ..., n_s \tag{7}$$

$$\mathscr{P}^i_{so} = \frac{\mu_0 \cdot h_{so}}{w_{so}} \cdot l_{fe} \qquad \text{for} \quad \text{i} = 1, 2, ..., n_s \tag{8}$$

where l_{fe} is the machine stack length, μ_0 is the vacuum permeability, μ_{fe-sy}, μ_{fe-st} and μ_{fe-ts} are the relative permeability of the stator yokes, teeth and tooth shoes (which depends on the BH curve working point of each tooth, tooth shoe or yoke). l_t, l_{ts}, l_{so} , w_t, w_{ts} and w_{so} are the tooth, tooth shoe and slot opening lengths and widths respectively, whereas l_y and w_y are the yoke length and thickness.

The rotor can be described by one non-linear permeance for each iron flux guide when only the d-axis is supplied:

$$\mathscr{P}^i_{ry} = \frac{\mu_0 \cdot \mu^i_{fe-rot} \cdot h^i_{fe}}{s^i_{fe}} l_{fe} \quad \text{for} \quad \text{i} = 1, 2, ..., n_r \tag{9}$$

where h_{fe} and s_{fe} are the height and length of each rotor island, μ_{fe-rot} is the relative permeability of the rotor flux guides whose number is equal to n_r.

B. q-axis MEC

When considering the q-axis current supply scenario, the stator MEC part remain almost the same while the rotor one has to model a different flux paths distribution as shown in Fig. 4. Indeed, the flux tubes cross the flux barriers and the iron ribs and these can be modeled by the permeances $\mathscr{P}^i_b$, $\mathscr{P}^i_r$:

$$\mathscr{P}^i_b = \frac{\mu_0 \cdot s^i_b}{h^i_b} \cdot l_{fe} \qquad \text{for} \quad \text{i} = 1, 2, ..., n_r - 1 \tag{10}$$

$$\mathscr{P}^i_r = \frac{\mu_0 \mu^i_{fe-rib} \cdot w^i_r}{h^i_b} \cdot l_{fe} \quad \text{for} \quad \text{i} = 1, 2, ..., n_r - 1 \tag{11}$$

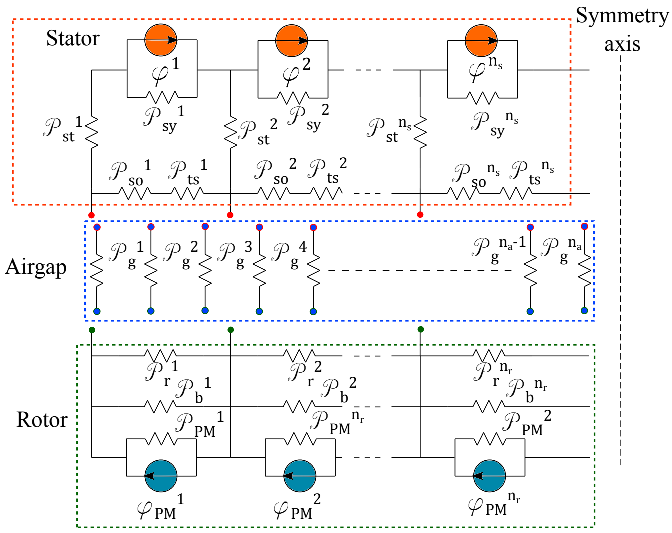

Fig. 4: Magnetic equivalent circuit for the q-axis flux path.

where h_b^i and s_b^i are the height and per unit surface of each flux barrier, μ_{fe-rib}^i and w_r are the permeability and width of each structural iron rib.

When considering the PMs within the rotor flux barriers, their presence can be modeled by the permeance $\mathscr{P}_{PM}^i$ and the flux generators φ_{PM}^i calculated as:

$$\mathscr{P}_{PM}^i = \frac{\mu_0 \cdot \mu_{PM} \cdot w_{PM}^i}{h_b^i} \cdot l_{fe} \quad \text{for} \quad \mathrm{i} = 1, 2, ..., n_r - 1 \tag{12}$$

$$\varphi_{PM}^i = B_r \cdot w_{PM}^i \cdot l_{fe} \qquad \text{for} \quad \mathrm{i} = 1, 2, ..., n_r - 1 \tag{13}$$

where w_{PM} and μ_{PM} are the PM width and linear relative permeability and B_r is PM residual flux density. These parameters depends on the adopted PM material.

C. Stator-rotor interface modeling

The airgap can be described by several linear permeances whose expression is:

$$\mathscr{P}_g^i = \frac{\mu_0 \cdot \Delta\alpha \cdot r_r}{g} \cdot l_{fe} \qquad \text{for} \quad \mathrm{i} = 1, 2, ..., n_a \tag{14}$$

where r_r is the airgap radius, g is the airgap thickness, $\Delta\alpha$ is an angle which depends on the number of considered airgap discretizations per half pole n_a:

$$\Delta\alpha = \frac{\pi}{2p \cdot n_a} \tag{15}$$

Once the machine geometry is defined, the connection criteria between stator and airgap networks and between rotor and airgap ones has to be defined.

In particular, the following rules based on the relative position of each airgap reluctance with respect to the stator slot pitch and the angular span between two adjacent rotor flux guides have been adopted.

- Stator-airgap connections: if the i^{th} airgap reluctance lies within the first tooth angular span (i.e. the angle between the middle of the k^{th} and $(k+1)^{th}$ slot opening), it is connected to the tooth node between the two adjacent slots;
- Rotor-airgap connections: if the i^{th} airgap reluctance lies within the first rotor island angular span (i.e. the angle between the middle of the k^{th} and $(k+1)^{th}$ flux barrier), it is connected to the tooth node between the two adjacent barriers.

Fig. 5 reports an example of the stator-rotor interface modeling adopting this approach which allows generalizing the interface between stator and rotor whatever number of stator slots and rotor flux barriers as will be shown in Section III.

The selection of the number of airgap subdivision n_a should be performed according to the stator slot - rotor barriers combination. Supposing a uniform distribution of the equivalent rotor slots, the minumum airgap subdivision per half pole can be identified as:

$$n_{a-min} = \frac{2\pi/4p}{\gcd(\alpha_{stat}/2, \alpha_{rot}/2)} \tag{16}$$

where α_{stat} and α_{rot} are the stator and rotor slot pitch, respectively. Adopting this approach allows modeling all the flux paths between each stator tooth and the closest rotor flux guides. As a consequence, when n_a is equal to n_{a-min} or its multiple, the estimation accuracy is greatly improved. The influence of this parameter on the estimation error will be analyzed in Section III-C.

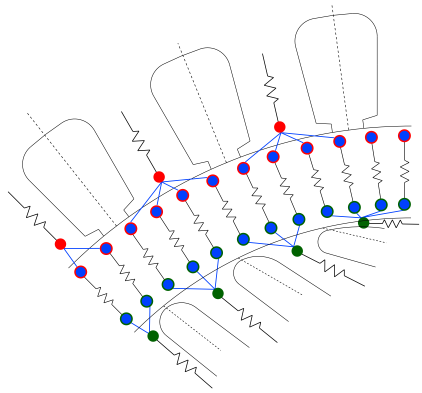

Fig. 5: Circuital modeling of the airgap region.

D. Resolution of the MECs

Both MECs can be solved by applying the nodal-voltage method. The relationships between node magnetic potentials, permeances and flux generators $\mathbf{\Phi}$ can be written with the following matrix equation (17):

$$\mathbf{P} \cdot \mathbf{V} = \mathbf{\Phi} \tag{17}$$

where $\mathscr{P}$ is the permeance matrix and V represents the voltage at each network node. The diagonal elements of $\mathscr{P}$ are the sum of the permeances which are connected to the i^{th} node, whereas the off-diagonal terms are the negative sum of the permenances between the i^{th} and j^{th} nodes.

The permeance matrix $\mathscr{P}$ has $[n_N \text{ x } n_N]$ dimensions, with n_N the number of MEC nodes, and can be found by the following relationship [21]:

$$\mathscr{P} = \mathbf{L^T}(\mathscr{P}_{lin} + \mathscr{P}_{fe} \cdot \mu_{\mathbf{fe}})\mathbf{L} \tag{18}$$

In (18) L is the incidence matrix (having size $[n_B \text{ x } n_N]$ where n_B is the number of branches) and determines the relation between each branch and the associated nodes: if the supposed direction of the flux in the i^{th} branch goes out from the j^{th} node, its value is 1, whereas if it goes in it its value is -1, otherwise it is 0. The matrix $\mathscr{P}_{lin}$ includes the permeances of the linear elements (i.e. airgap, slot opening and flux barrier), whereas the matrix $\mathscr{P}_{fe}$ include the permeances of the non-linear machine parts. The matrices $\mathscr{P}_{lin}$ and $\mathscr{P}_{fe}$ (whose dimensions are ($[n_B \text{ x } n_B]$) are diagonal matrix whose elements are the permeances of each branch without considering the relative permeability, whereas $\mu_{\mathbf{fe}}$ ($[n_B \text{ x } n_B]$) is the relative permeability matrix which has to be identified iteratively.

The presence of the non-linear elements implies the need of an iterative solving procedure as the Newton-Raphson method. Indeed, the operating point of the non-linear reluctances (i.e. stator teeth e yokes, rotor yokes) have to be identified by solving the MEC at each iteration step thus updating the permeabilities for the next step. The non-linear problem can be formulated as follows:

$$\mathbf{r} = \mathscr{P} \cdot \mathbf{V} - \mathbf{\Phi} \tag{19}$$

where $\mathbf{r}$ is the residual which has to be reduced using the iterative procedure. The nodal voltage solution at the $k+1$ iteration step can be obtained using (20).

$$\mathbf{V}(k+1) = \mathbf{V}(k) - \mathbf{J}(k)^{-1}\mathbf{r}(k) \tag{20}$$

where $\mathbf{J}(k)$ is the Jacobian matrix at the step k, which can be calculated as [21]:

$$\mathbf{J} = \mathscr{P} + \mathbf{L^T}(\mathscr{P}_{fe} \cdot \mathbf{A} \cdot \dot{\mu}_{\mathbf{fe}})\big((\mathbf{L V_d U}) \cdot \mathbf{L}\big) \tag{21}$$

where $\mathbf{A}$ is the flux-crossed area of the non-linear elements, $\dot{\mu}_{fe}$ is a diagonal matrix ($[n_B$ x $n_B]$) whose elements are the derivative of the relative permeability with respect to the its associated magnetic field intensity H. $\mathbf{V_d}$ is a diagonal matrix of the nodal voltages $\mathbf{V}$, whereas $\mathbf{U}$ is a ($[n_N$ x $n_N]$) matrix describing the connections between each node (i.e. if the i^{th} and j^{th} nodes are connected is 1, otherwise is 0).

The procedure can be therefore summarized as follows:

1) First, the machine operating point is defined (i.e $i_d - i_q$).
2) The linear matrixes $\mathscr{P}_{lin}$ and $\mathscr{P}_{fe}$ can be predetermined as they only depend on the machine geometry.
3) For the first iteration, an arbitrary solution in terms of nodal voltages $\mathbf{V}(k)$ has to be imposed.
4) The calculation of the permeability matrix ($\mu_{\mathbf{fe}}$) can be performed.
5) $\mu_{\mathbf{fe}}$ is used for to the computation of $\mathscr{P}$ as in (18). Then (19) is used to calculate the residual $\mathbf{r}$.
6) The Jacobian matrix can be calculated as in (21), therefore the solution $\mathbf{V}(k+1)$ can be updated.
7) The latter is used to update the permeability matrix ($\mu_{\mathbf{fe}}$).
8) The procedure re-starts from point 4 until $\mathbf{r}$ lies within a predefined threshold.

Once the above procedure has been applied, from the nodal voltage vector is possible to calculate the flux in each branch including the airgap branch and so the airgap flux density B_g as function of the angular position can be derived. Finally, it is possible to calculate the d- and q-axis flux linkages by integrating the d- and q-axis waveform of B_g as in (22) and (23):

$$\lambda_d(i_d, 0) = \frac{k_w N_s D_i l_{fe}}{p} \cdot \int_{\frac{\pi}{2}}^{\frac{3}{2}\pi} B_g(i_d, 0) d\theta_{el} \tag{22}$$

$$\lambda_q(0, i_q) = \frac{k_w N_s D_i l_{fe}}{p} \cdot \int_{0}^{\pi} B_g(0, i_q) d\theta_{el} \tag{23}$$

where k_w is the winding factor, N_s is turns' number in series per phase, D_i is the airgap diameter and θ_{el} is the electrical angular position.

III. Analytical prediction and FE validation

The above described procedure has been applied to analyse machines featuring different stator and rotor layouts with and without permanents magnets in order to verify its efficacy in predicting the performance over a wide operating range.

TABLE I: Machine parameters

Parameter	Value	Units
Outer stator radius	130	mm
Airgap radius	84.5	mm
Stack length	205	mm
Pole pair	2	/
Stator slots	24/48	/
Airgap thickness	0.5	mm
N° of flux barriers	2/3/4	/

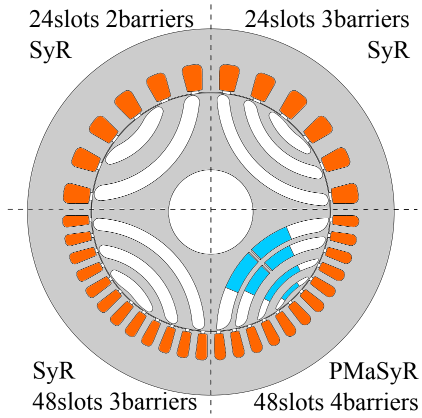

Fig. 6: Machines cross-sections.

The main parameters of the analysed machines are reported in Table I while Fig. 6 depicts their cross-sections. In the following subsections, the airgap flux densities prediction when supplying only with d- or q-axis current are analytically estimated and compared with the respective FE ones. Then, the flux linkages, torque and internal power factor predictions as function of the current level are compared with the respective FEAs.

A. *Airgap flux densities*

Fig. 7 and Fig. 8 reports a comparison between the analytical and FE computations of the d-axis and q-axis airgap flux density for two load conditions as function of the electrical angle θ_{el} for the four considered machines. The same figures also reports the first harmonics of the analytical and FEA predictions as dashed lines. It is clear that the analytical model is able to accurately predict the first harmonic of the airgap flux density independently from the supply (d- or q-axis current) and saturation condition. It is obvious and evident that the slotting effect is not fully captured by the equivalent magnetic circuits. Despite that, the quality of the estimation is not affected by the slots/barriers combination thus assuring the generality of the proposed circuital models. It is worth to highlight the phase error between the first harmonic of the estimated and FE d-axis airgap flux densities when considering a PMaSyR machine (Fig. 7g and h). The proposed model consider two separate circuits to represent the d- and q-axis supply conditions; as a consequent it is unable to predict the machine behaviour when both axis are excited at the same time. This inability becomes evident when analysing a

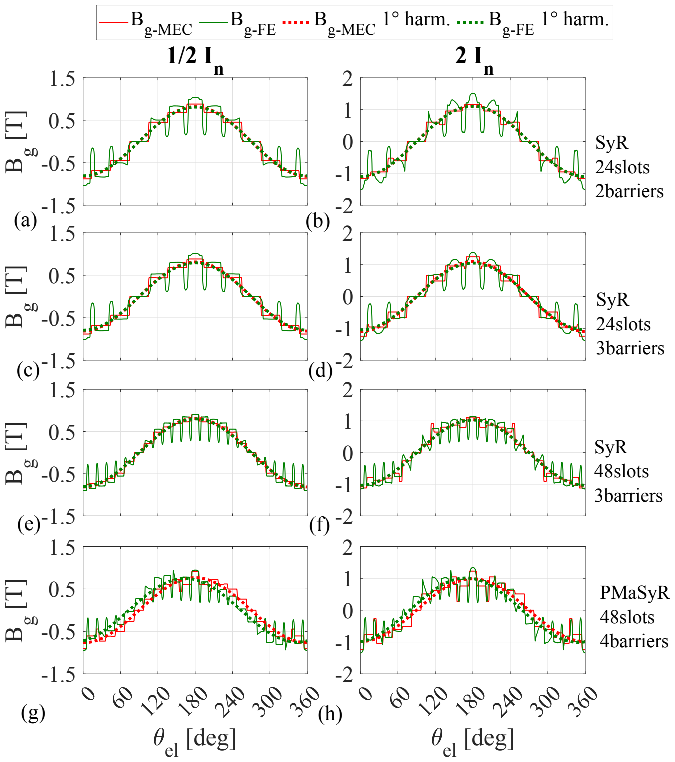

Fig. 7: Analytical and FE airgap flux densities as function of the electrical angle for different machines and d-axis current.

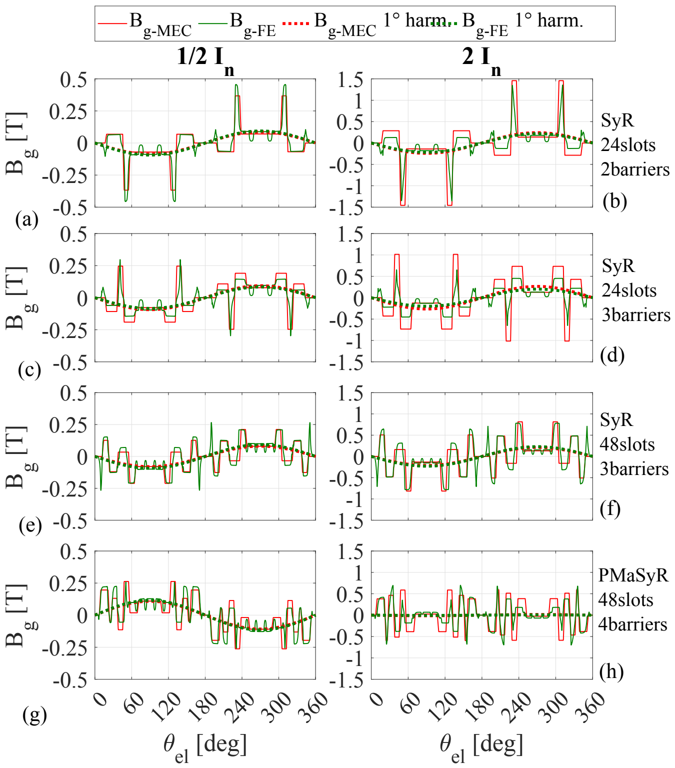

Fig. 8: Analytical and FE airgap flux densities as function of the electrical angle for different machines and q-axis current.

PMaSyR machine. Indeed, the FEA carried out to predict the d-axis flux density consider the permanent magnets while the d-axis MEC does not consider them.

B. Airgap discretization sensitivity analysis

As mentioned in Section II-C, the parameter n_a defining the airgap discretization in the MEC is particularly important as it greatly affects the estimation accuracy. In the following a sensitivity analysis is reported with the twofold aim of assessing the trade-off between accuracy of the prediction and computational time and validate the proposed formulation (16) to calculate the minimum number of airgap subdivision n_{a-min}. Fig. 9 reports the percentage error between the MEC and FE computation of first harmonic of the airgap flux density B_g when supplying the d-axis circuit at rated condition, as function of n_a for three SyR machines. It is evident that it is not necessary to increase the airgap subdivision above the required minimum as it does not lead to better result but only worsens the computational burden. As expected, the latter increases with n_a but in any case remains below 0.15s (at n_{a-min}). It is worth to underline that the sensitivity analysis has been performed for different stator slots - rotor flux barriers combinations, including an "unfortunate" one where the minimum n_a is high (Fig. 9c). Also in this case, the computational time is comparable with the other ones (at n_{a-min}), i.e. there is no drastic increment.

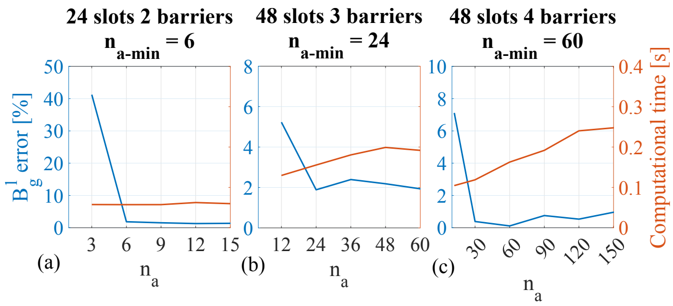

Fig. 9: Error between MEC and FE computation of the first harmonic of B_g and computational burden as function of the airgap subdivision.

C. Flux linkage

Once the airgap flux densities are known, the flux linkages can be calculated using (22) and (23) for different current levels. The results of the above calculations are show in Fig. 10 for all the considered machines. It is worth to notice the excellent agreement between the MEC and the FE computation of both $\lambda_d(i_d, 0)$ and $\lambda_q(0, i_q)$, regardless the slots/barriers combination even when considering the PM assisted scenario.

The described MEC model is not capable of accounting for the cross-saturation effects, which is relevant when considering high anisotropic synchronous machines. Indeed, the d-axis flux linkage as function of the i_d current would decrease when the q-axis current increases as well as the q-axis one would decrease as i_d increases.

D. Torque and internal power factor

The effects of the such approximation (i.e. the neglected cross-coupling effects) can be depiced in Fig. 11 and 12 where the comparison between MEC and FE computation of both average torque and internal power factor are shown for only one SyR case (48 slots-3 barriers) for the sake of brevity and

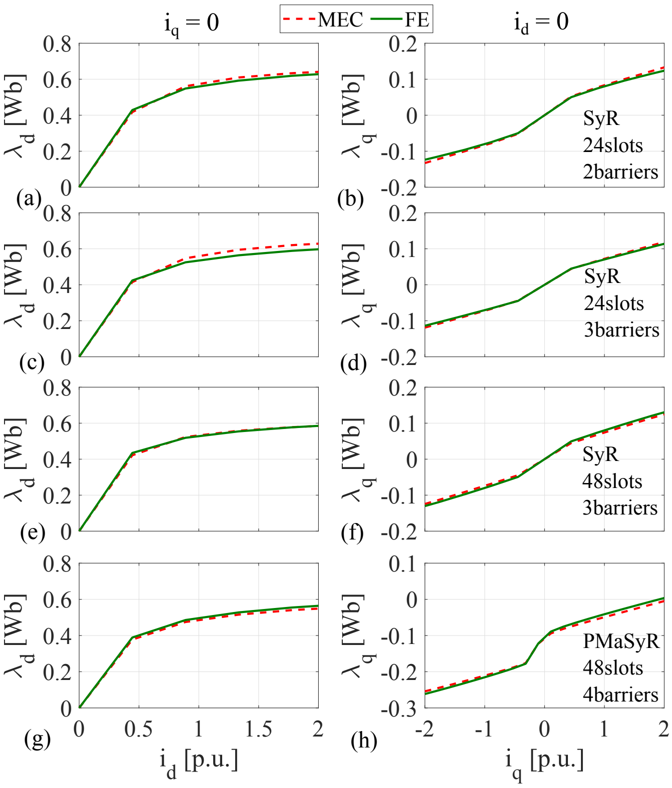

Fig. 10: Comparison between analytical and FE computations of (a) d-axis flux linkage vs current amplitude, (b) q-axis flux linkage vs current amplitude

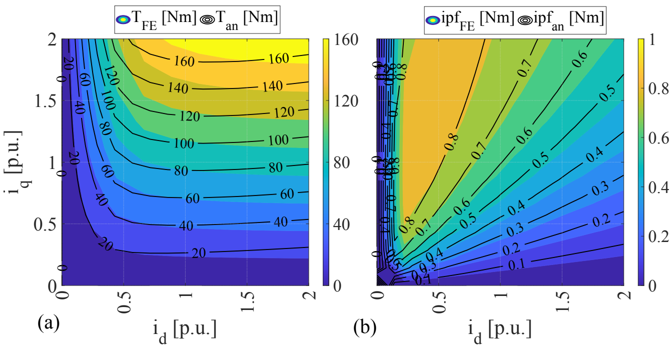

Fig. 11: Comparison between analytical and FE computations of (a) average torque and (b) internal power factor maps considering the 48 slots-3 barriers SyR case.

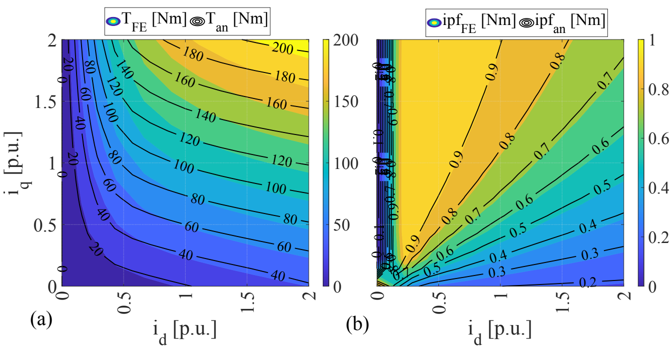

Fig. 12: Comparison between analytical and FE computations of (a) average torque and (b) internal power factor maps of the considered PMaSyR machine.

the PMaSyR case respectively. The amount of such estimation errors increases from the bottom left to the top right corner of the $i_d - i_q$ plane since in that direction the cross-coupling becomes more pronounced.

IV. Magnetic model FE correction procedure

With the aim of accounting for the cross-couplings effects and therefore obtaining a good estimation of both average torque and power factor in the whole d-q current plane, a magnetic model correction procedure is proposed and detailed in this section. In particular, few operating points from the $i_d - i_q$ plane are selected and analysed using magneto-static FE simulations. In particular five points are selected (i_d^*, i_q^*): four close to the corners and one in the middle of the d-q current plane. The placement of these points is carried out to uniformly cover the d-q current plane. The calculated FE d- and q-axis flux linkages are then divided by the respective analytical estimations as in (24) and (25):

$$k_d(i_d^*, i_q^*) = \frac{\lambda_{dFEA}(i_d^*, i_q^*)}{\lambda_{dAN}(i_d^*, 0)} \tag{24}$$

$$k_q(i_d^*, i_q^*) = \frac{\lambda_{qFEA}(i_d^*, i_q^*)}{\lambda_{qAN}(0, i_q^*)} \tag{25}$$

These factors embed the cross-coupling effect in terms of flux linkage deviation for the simulated operating points. Such knowledge is then extended to the overall $i_d - i_q$ plane using a linear interpolation allowing to calculate the flux linkage including the cross-coupling as simple product between the analytical estimation and the respective adjustment factor:

$$\lambda_d(i_d, i_q) = \lambda_{dAN}(i_d, 0) \cdot k_d(i_d, i_q) \tag{26}$$

$$\lambda_q(i_d, i_q) = \lambda_{qAN}(0, i_q) \cdot k_q(i_d, i_q) \tag{27}$$

The results of the magnetic model correction procedure applied to the SyR case are shown in Fig. 13 for the d- and q-axis flux linkages. Each figure shows the comparison between the analytical estimation of the flux linkage with the respective FE computation, the adjustment factor and the comparison between the adjusted flux linkage and the FE counterpart. The last sub-figures show an excellent agreement between FE and adjusted flux linkage leading to a better estimation of the average torque and internal power factor over the entire d-q current plane as shown in Fig. 14. Obviously the estimation error decreases as the number of FE-simulated operating points increases. Fig. 15 reports the torque comparison when considering 7 operating points in the d-q current plane to calculate the adjustment factors.

When considering the PMaSyR scenario, the FE correction procedure must be slightly modified to deal with the condition related to the possible change of sign of the q-axis flux. To do so, the q-axis correction factor has to be calculated as:

$$k_q'(i_d^*, i_q^*) = \frac{\lambda_{qFEA}(i_d^*, i_q^*) + C}{\lambda_{qAN}(0, i_q^*) + C} \tag{28}$$

where C is an arbitrary constant so that $\lambda_{qAN}(0, i_q^*) + C > 0$. In this case, the adjusted analytical estimation of the q-axis flux becomes:

$$\lambda_q(i_d, i_q) = (\lambda_{qAN}(0, i_q) + C) \cdot k_q'(i_d, i_q) - C \tag{29}$$

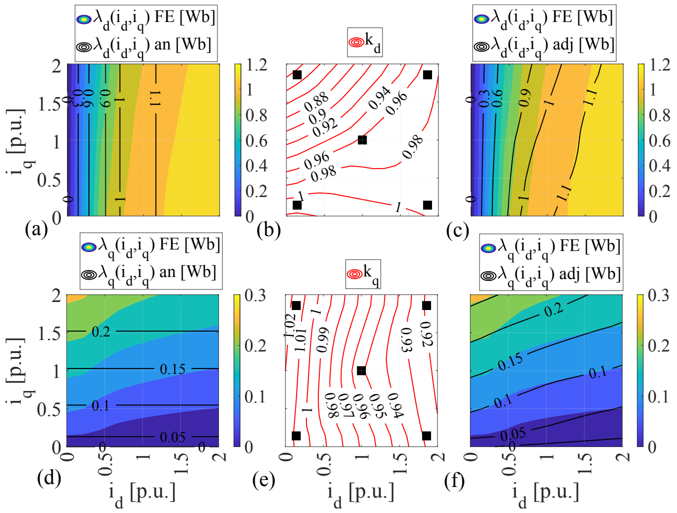

Fig. 13: d-axis and q-axis flux linkages estimation for the 48 slots-3 barriers SyR machine: (a,d) analytical and FE computation, (b,e) adjustment factor, (c,f) analytically-adjusted and FE computations.

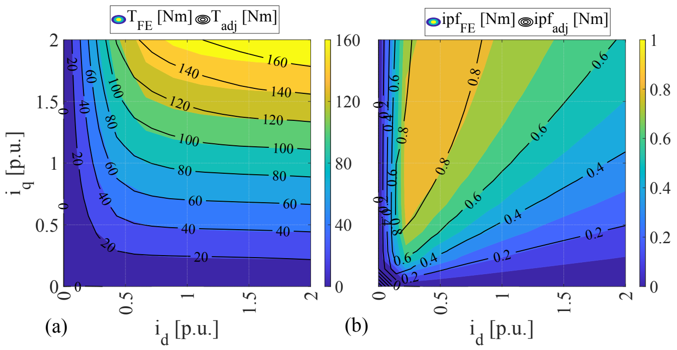

Fig. 14: Comparison between analytically-adjusted and FE computations of (a) average torque and (b) internal power factor maps for the 48 slots-3 barriers SyR machine.

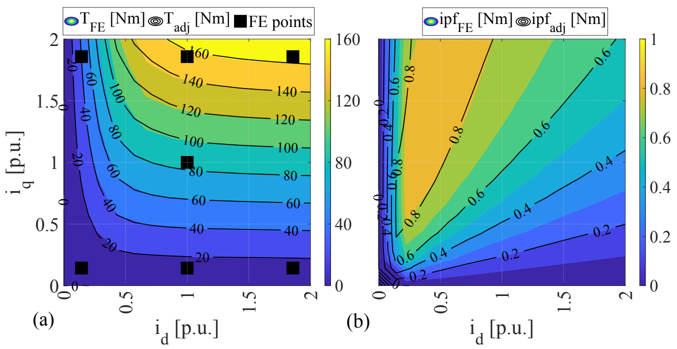

Fig. 15: Comparison between analytically-adjusted and FE computations of (a) average torque and (b) internal power factor maps for the 48 slots-3 barriers SyR machine when the adjustment factors are calculated with 7 static FEAs.

Fig. 16 shows the analytical and adjusted estimation of the flux linkages along with the adjusted factors over the dq plane for the PMaSyR scenario. An excellent estimation can be observed, also in terms of of torque and power factor as shown in Fig. 17.

Table II reports the estimations errors of both torque (e_T) and internal power factor (e_{ipf}) for two considered geometries

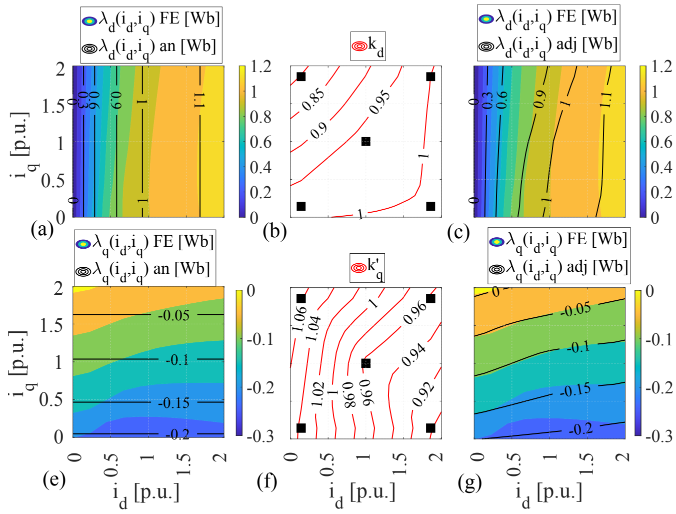

Fig. 16: d-axis and q-axis flux linkages estimation for the 48 slots-3 barriers PMaSyR machine: (a,d) analytical and FE computation, (b,e) adjustment factor, (c,f) analytically-adjusted and FE computations.

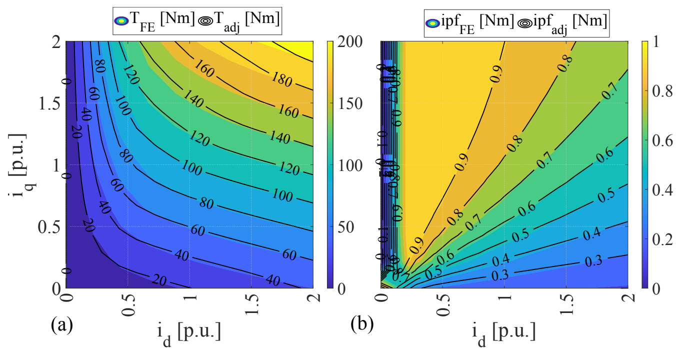

Fig. 17: Comparison between analytically-adjusted and FE computations of (a) average torque and (b) internal power factor maps for the PMaSyR machine.

TABLE II: Estimation errors and computational times

	SyR 48/3	**PMaSyR 48/4**
$\max(e_T)$ [%]	6 (18)	5 (20)
$\mathrm{avg}(e_T)$ [%]	1 (5)	1 (4)
$\max(e_{ipf})$ [%]	2 (16)	1 (4)
$\mathrm{avg}(e_{ipf})$ [%]	0.2 (4.5)	0.1 (1)
FEA [s]	500	600
Hybrid [s]	27	32

in term of maximum and average values in the d-q current plane. The values reported in round brackets refer to the error of the pure analytical estimations. As already mentioned, the proposed hybrid approach allows to drastically reduce the estimation error compared to the full analytical approach but with a much lighter computational burden respect to the full FE mapping. The same table - in the last two rows - shows the computational time of the full FEA and proposed approach when mapping with a 10x10 grid the d-q current plane. The presented performance estimation methodology is approximately 18 times faster than the respective full FEA (with a workstation Z420 Xeon 3,6 GHz with 12GB of RAM).

V. Experimental assessment

The proposed hybrid analytical-FE performance estimation approach has been validated comparing its prediction with a more comprehensive FEA. This validation exercise has been performed considering different machine geometries including the PM assistance. To further strengthen the effectiveness of the proposed performance estimation methodology, its predictions have been compared with the measurements carried out on a SyRM prototype (available in the university facility) rated 15kW and whose details are reported in Table I (48 slots and 4 rotor flux barriers).

The experimental platform is shown in Fig. 18 where it can be seen that the SyR machine under the test is mechanically coupled with a commercial induction motor drive via a Kistler 4503A torque sensor which provides an accurate torque measurement. The SyR machine is fed by a two-level IGBT voltage inverter (Semikron SKAI) connected to a variable voltage DC link (voltage is set at 540 V). The control algorithms are implemented using the fast prototyping platform dSpace MicroLabBox (DS1202) connected to the inverter through an interface board. The sampling frequency is set equal to the switching frequency at 10 kHz with a dead-time of 4μs.

The constant speed magnetic model identification method [22] has been implemented to obtain the flux linkage and the torque maps. This experimental magnetic model approach has been adopted as it does not requires the knowledge of the stator resistance, compensate the temperature variation of the such parameter, does not need the voltage measurements and any inverter non-linearity compensation. This procedure performs the identifications of the flux linkage components for every point in the d-q axis current plane via a sequence of tests carried at constant speed imposed by the prime mover while the motor under test is current controlled. The speed of the prime mover is set to one-third of the base speed of the SyRM under the test, namely 500 rpm in this case, in order to minimize the influence of iron loss and provide a good signal-to-noise ratio. The flux linkages for each d-q current combination are estimated using the d- and q-axis reference

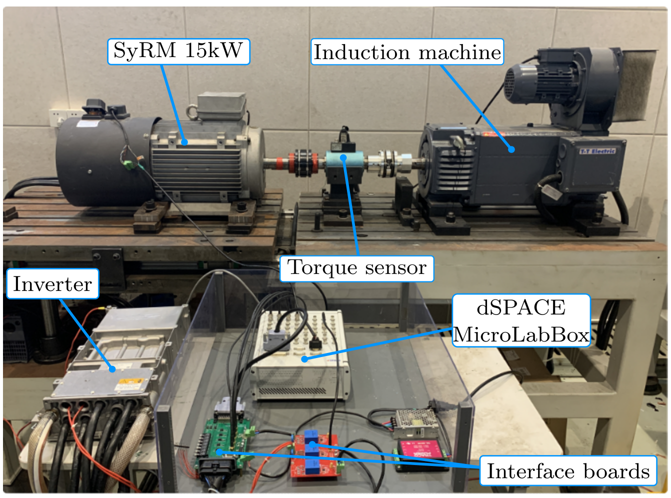

Fig. 18: Experimental setup.

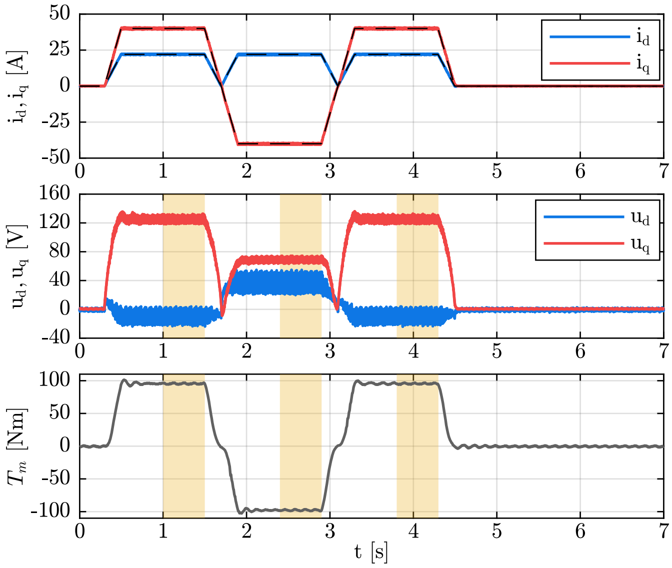

Fig. 19: Example of current and voltage waveforms during the identification with highlighted data log windows.

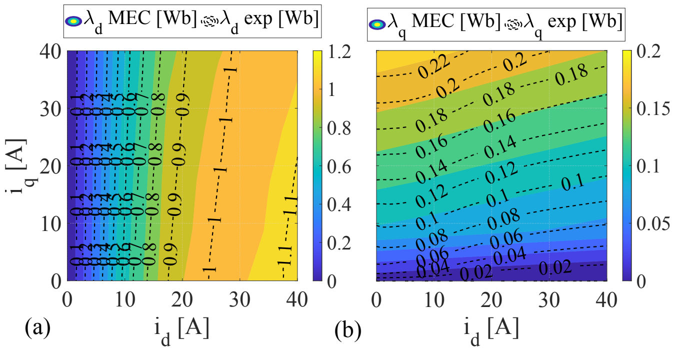

Fig. 20: Comparison between analytically-adjusted and experimental computations of (a) d-axis and (b) q axis flux linkages maps.

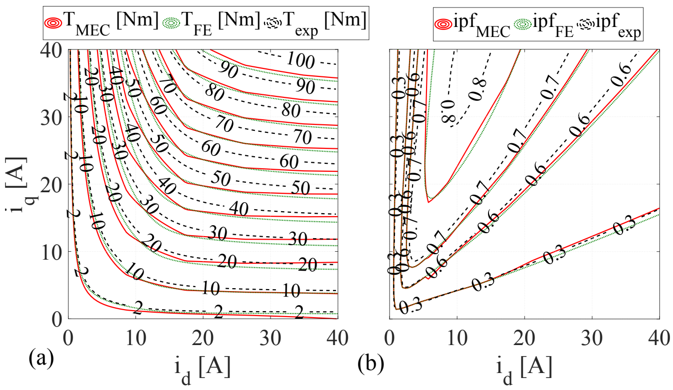

Fig. 21: Comparison between analytically-adjusted, fe and experimental computations of (a) average torque and (b) internal power factor maps.

voltage during three tests carried out in motoring, generating and motoring mode respectively as shown in Fig. 19.

The ploy of using the first two pulses avoid the knowledge of the stator resistance while the third one allows compensating the temperature resistance variation. The steady-state values of the reference voltages are calculated by averaging the measurements over a mechanical period after the transient has diminished in order to eliminate the effects of the spatial harmonics and inverter dead-time, as shown Fig.19.

Fig. 20 reports the comparison between the measurements and the estimated d- and q-axis flux linkages showing a good agreement which leads to an excellent prediction of both average torque and internal power factor shown in Fig. 21. The maximum torque error is 13% whereas the average one is 6%. In terms of internal power factor, the maximum error is 4.3% while the average one is 2.5%. The higher errors - respect to the one shown in Table II - are due to mismatch between the modelled geometry (and material behaviour) and the real one. Indeed, the FEA provide almost the same results of the proposed hybrid model as shown in Fig. 21.

VI. Conclusion

This paper has proposed an accurate hybrid FE-analytical model for synchronous reluctance machines with and without permanent magnet assistance capable of accounting all the machine non-linearity. A couple of magnetic equivalent circuits solved in a non-linear fashion allows considering the saturation while the cross-saturation is accounted by FE-simulating few selected operating point in $i_d - i_q$ plane. The method allows to obtain an overall excellent estimation of the direct and quadrature axis flux linkages for a wide range of machine operating conditions including the overload ones. Its effectiveness has been confirmed considering different machine geometries with various combinations of rotor flux barriers and stator slots. It requires a negligible computational burden when compared to a full-FEA approach. Given its computational efficacy, the proposed approach can be used both for analysis and design purposes. Indeed, the full computation of the entire d-q current plane requires only five (or seven according to the required accuracy) static finite element simulations.

References

[1] M. Popescu, J. Goss, D. A. Staton, D. Hawkins, Y. C. Chong, and A. Boglietti. Electrical vehicles—practical solutions for power traction motor systems. *IEEE Transactions on Industry Applications*, 54(3):2751–2762, 2018.

[2] L. Shao, A. E. H. Karci, D. Tavernini, A. Sorniotti, and M. Cheng. Design approaches and control strategies for energy-efficient electric machines for electric vehicles—a review. *IEEE Access*, 8:116900–116913, 2020.

[3] N. Tang, D. Sossong, N. Krause, X. Hou, M. J.T. Liben, D. C. Ludois, and I. P. Brown. Implementation of a metamodel-based optimization for the design of a high power density wound field traction motor. *IEEE Transactions on Industry Applications*, 59(6):6726–6735, 2023.

[4] T. Zou, D. Gerada, S. La Rocca, A. La Rocca, A. Walker, G. Vakil, S. L. Arevalo, M. Xu, Z.and Cui, A. Bardalai, M. Wang, R. M. R. Kumar, A. Marfoli, K. Paciura, R. Barden, E. Ernest, S. Zhu, N. Qayyum, A. McQueen, F. Zhang, and C. Gerada. Airgap length analysis of a 350 kw pm-assisted syn-rel machine for heavy duty ev traction. *IEEE Transactions on Industry Applications*, 59(2):1557–1570, 2023.

[5] B. Praslicka, C. Ma, and N. Taran. A computationally efficient high-fidelity multi-physics design optimization of traction motors for drive cycle loss minimization. *IEEE Transactions on Industry Applications*, 59(2):1351–1360, 2023.

[6] G. Xu, Z. Jia, Q. Chen, J. Xia, Y. Cai, and Z. Zhang. A fast and effective optimization procedure for the ferrite pmasynrm to reduce material cost. *IEEE Transactions on Transportation Electrification*, pages 1–1, 2023.

[7] Young-Hoon Jung, Min-Ro Park, Ki-O Kim, Jun-Woo Chin, Jung-Pyo Hong, and Myung-Seop Lim. Design of high-speed multilayer ipmsm using ferrite pm for ev traction considering mechanical and electrical characteristics. *IEEE Transactions on Industry Applications*, 57(1):327–339, 2021.

[8] M. Di Nardo, G. Gallicchio, M. Palmieri, A. Marfoli, M. Degano, C. Gerada, and F. Cupertino. High speed permanent magnet assisted synchronous reluctance machines – part ii: Performance boundaries. *IEEE Transactions on Energy Conversion*, 37(4):2567–2577, 2022.

[9] G. Pellegrino, F. Cupertino, and C. Gerada. Automatic design of synchronous reluctance motors focusing on barrier shape optimization. *IEEE Transactions on Industry Applications*, 51(2):1465–1474, 2015.

[10] A. Vagati, G. Franceschini, I. Marongiu, and G. P. Troglia. Design criteria of high performance synchronous reluctance motors. In *Industry Applications Society Annual Meeting, 1992., Conference Record of the 1992 IEEE*, pages 66–73 vol.1.

[11] A. Tessarolo. Modeling and analysis of synchronous reluctance machines with circular flux barriers through conformal mapping. *Magnetics, IEEE Transactions on*, 51(4):1–11, April 2015.

[12] M. Murataliyev, M. Degano, and M. Galea. A novel sizing approach for synchronous reluctance machines. *IEEE Transactions on Industrial Electronics*, 68(3):2083–2095, 2021.

[13] H. Mahmoud, N. Bianchi, and N. Bacco, G.and Chiodetto. Nonlinear analytical computation of the magnetic field in reluctance synchronous machines. *IEEE Transactions on Industry Applications*, 53(6):5373–5382, 2017.

[14] A. M. Silva, C. H. Antunes, A. M. S. Mendes, and F. J. T. E. Ferreira. Generalized reluctance network framework for fast electromagnetic analysis of radial-flux machines. *IEEE Transactions on Energy Conversion*, pages 1–11, 2022.

[15] O. Korman, M. Di Nardo, M. Murataliyev, M. Degano, and C. Gerada. Magnetic equivalent circuit modelling of synchronous machines. In *2023 IEEE International Electric Machines & Drives Conference (IEMDC)*, pages 1–7, 2023.

[16] L. Ding, G. Liu, Q. Chen, and G. Xu. A novel mesh-based equivalent magnetic network for performance analysis and optimal design of permanent magnet machines. *IEEE Transactions on Energy Conversion*, 34(3):1337–1346, 2019.

[17] A. Vagati, B. Boazzo, P. Guglielmi, and G. Pellegrino. Design of ferrite-assisted synchronous reluctance machines robust toward demagnetization. *IEEE Transactions on Industry Applications*, 50(3):1768–1779, 2014.

[18] S. Ferrari and G. Pellegrino. Feafix: Fea refinement of design equations for synchronous reluctance machines. *IEEE Transactions on Industry Applications*, 56(1):256–266, 2020.

[19] Seok-Hee Han, Thomas M. Jahns, and Wen L. Soong. A magnetic circuit model for an ipm synchronous machine incorporating moving airgap and cross-coupled saturation effects. In *2007 IEEE International Electric Machines & Drives Conference*, volume 1, pages 21–26, 2007.

[20] G. Gallicchio, F. Cupertino, M. Di Nardo, M. Degano, and C. Gerada. Hybrid fe-analytical procedure for fast flux map computation of permanent magnets assisted synchronous reluctance machines. In *2023 IEEE International Electric Machines & Drives Conference (IEMDC)*, pages 1–7, 2023.

[21] A. Hemeida, A. Lehikoinen, P. Rasilo, H. Vansompel, A. Belahcen, A. Arkkio, and P. Sergeant. A simple and efficient quasi-3d magnetic equivalent circuit for surface axial flux permanent magnet synchronous machines. *IEEE Transactions on Industrial Electronics*, 66(11):8318–8333, 2019.

[22] E. Armando, R. I. Bojoi, P. Guglielmi, G. Pellegrino, and M. Pastorelli. Experimental identification of the magnetic model of synchronous machines. *IEEE Trans. Ind. Appl.*, 49(5):2116–2125, 2013.

Gianvito Gallicchio received the B.Sc. (Hons.), M.Sc. (Hons.) and the Ph.D. degrees in electrical engineering from the Politecnico di Bari, Bari, Italy in 2016, 2018 and 2023 respectively. He is currently a research fellow with the Electrical Machines and Drives Group, Politecnico di Bari. His main research interests include the analysis, modeling and design optimization of permanent magnet and synchronous reluctance machines for both traction and high-speed applications.

Mauro Di Nardo (M'18) received the M.Sc. (Hons.) degree in electrical engineering from the Polytechnic University of Bari, Italy, in 2012, and the Ph.D. degree in electrical machine design from the University of Nottingham, U.K., in 2017. From 2017 to 2019, he was with the AROL spa leading the R&D team focusing on electrical drives design for mechatronics applications. Between 2019 and 2023, he was with the Power Electronics and Machine Control Group of the University of Nottingham as Research Fellow. He is currently an assistant professor in electrical machine and drives at the Polytechnic University of Bari, Italy. He serves as an Associate Editor for the IEEE Open Journal of Industry Applications and IEEE Transactions on Energy Conversion.

Francesco Cupertino (M'08–SM'12) received the Laurea and Ph.D. degrees in electrical engineering from the Politecnico di Bari, Bari, Italy, in 1997 and 2001, respectively. Since 2001, he has been with the Department of Electrical and Information Engineering, Politecnico di Bari, where he is currently a Full Professor of converters, electrical machines, and drives. He is the Scientific Director of several public/private laboratories at Politecnico di Bari that enroll more than 50 researchers. His research interests include the design of synchronous electrical machines, motion control of high performances electrical machines, applications of computational intelligence to control, and sensorless control of ac electric drives. He has authored or coauthored more than 160 scientific papers. F. Cupertino is currently the rector of the Politecnico di Bari.

Vasyl Varvolik received the B.Sc. and M.Sc. degrees in electrical engineering from the National Technical University of Ukraine "Igor Sikorsky Kyiv Polytechnic Institute," Kyiv, Ukraine, in 2016 and 2018, respectively. He secured the Ph.D. degree in electrical and electronics engineering with the University of Nottingham, Ningbo, China in 2023 where is currently a research fellow. His research interests include high-fidelity simulation, parameter identification, torque ripple reduction, high-performance control of synchronous reluctance, and permanent magnet synchronous motor drives.

Giampaolo Buticchi received the M.Sc. degree in electronic engineering and the Ph.D. degree in information technologies from the University of Parma, Parma, Italy, in 2009 and 2013, respectively. In 2012, he was a Visiting Researcher with the University of Nottingham, Nottingham, U.K. Between 2014 and 2017, he was a Postdoctoral Researcher with the University of Kiel, Kiel, Germany. He is currently a Professor of Electrical Engineering with the University of Nottingham, Ningbo, China.

Michele Degano (SM'21) received his Master's degree in Electrical Engineering from the University of Trieste, Italy, in 2011, and his Ph.D. degree in Industrial Engineering from the University of Padova, Italy, in 2015. Between 2014 and 2016, he was a research fellow at The University of Nottingham, UK, within the Power Electronics, Machines and Control (PEMC) Research Group. In 2016 he was appointed Assistant Professor within the same group, promoted Associate Professor in 2020 and full professor in 2023. His main research focuses on electrical machines and drives for industrial, automotive, railway and aerospace applications, ranging from small to large power.

Chris Gerada received the Ph.D. degree in numerical modeling of electrical machines from The University of Nottingham, Nottingham, U.K., in 2005. He was a Researcher with The University of Nottingham, working on high-performance electrical drives and on the design and modeling of electromagnetic actuators for aerospace applications. In 2008, he became a Lecturer in electrical machines, in 2011, as an Associate Professor, and in 2013, a Professor at The University of Nottingham. His main research interests include the design and modeling of high-performance electric drives and machines. He has secured major industrial, European and U.K. grants, authored more than 200 papers and was awarded a Royal Academy of Engineering Research Chair to consolidate research in the field.